

Exchange-Biased $\text{Fe}_{3-x}\text{O}_4$ -CoO Granular Composites of Different Morphologies Prepared by Seed-Mediated Growth in Polyol: From Core–Shell to Multicore Embedded Structures

Giulia Franceschin,^{*} Thomas Gaudisson, Nicolas Menguy, Brad C. Dodrill, Nader Yaacoub, Jean-Marc Grenèche, Raul Valenzuela, and Souad Ammar^{*}

Magnetically contrasted granular hetero-nanostructures are prepared by seed-mediated growth in polyol, properly combining two oxide phases with different magnetic order, ferrimagnetic (F) partially oxidized magnetite $\text{Fe}_{3-x}\text{O}_4$ and antiferromagnetic (AF) cobalt oxide. Spinel $\text{Fe}_{3-x}\text{O}_4$ nanoparticles are first synthesized and then used as seeds for rock salt CoO nanocrystals growth. Three different hetero-nanostructure designs are realized, acting on the content ratio between the seeds and the deposit's precursors during the synthesis. For all of them, the spinel and the rock salt phases are confirmed by X-ray diffraction and high-resolution transmission electron microscopy. Both phases are obtained in high-crystalline quality with a net epitaxial relationship between the two crystallographic lattices. Mössbauer spectrometry confirms the cobalt cation diffusion into the spinel seeds, giving favorable chemical interfacing with the rock salt deposit, thus prevailing its heterogeneous nucleation and consequently offering the best condition for exchange-bias (EB) onset. Magnetic measurements confirm EB features. The overall magnetic properties are found to be a complex interplay between dipolar interactions, exchange anisotropy at the F/AF interface, and magnetocrystalline anisotropy enhancement in the F phase, due to Co^{2+} diffusion into iron oxide's crystalline lattice. These results underline the powerfulness of colloidal chemistry for functional granular hetero-nanostructured material processing.

nanostructures that open up additional possibilities for manipulation of matter physical properties. It clearly enables the combination of different phases, providing a very powerful approach for the creation of smart materials with novel properties, not found in their own constituents.^[1] Indeed, the advantage of such materials lies not only in their multifunctionality, but also in the possibility to improve and tune the single-phase properties using the interactions between the different components.

Focusing on such heterostructures, several chemical strategies were employed to produce them, more or less successfully, with different morphologies. The major synthetic challenges stem from the non-trivial chemical and physical interfacing of the different phases in terms of their chemical compatibility and their crystallographic lattice accommodation.

One of the most promising colloidal processing approaches is the multistep synthesis. Presynthesized nanoparticles

(NPs), often by precipitation from a homogenous reaction solution, are used as seeds for the nucleation and growth of other crystalline material, the deposit. Such a colloidal-mediated growth technique is valuable if the separate nucleation of the

1. Introduction

Colloidal synthesis of inorganic nanocrystals gives an attracting opportunity to create a wide range of multicomponent

Dr. G. Franceschin,^[†] Dr. T. Gaudisson, Prof. R. Valenzuela, Prof. S. Ammar
ITODYS
Université Paris Diderot
Sorbonne Paris Cité, CNRS UMR-7086
15 rue Jean-Antoine de Baïf, 75013 Paris, France
E-mail: giulia.franceschin@univ-paris-diderot.fr;
ammarmar@univ-paris-diderot.fr

Prof. N. Menguy
IMPMC
Sorbonne Université
UMR CNRS 7590, MNHN, IRD
75005 Paris, France

 The ORCID identification number(s) for the author(s) of this article can be found under <https://doi.org/10.1002/ppsc.201800104>.

^[†]Present address: IPANEMA, CNRS, ministère de la culture et de la Communication, Université de Versailles Saint-Quentin-en-Yveline, USR 3461, Université Paris-Saclay, 91128 Gif-sur-Yvette, France

B. C. Dodrill
Lake Shore Cryotronics
575 McCorkle Blvd, Westerville, OH 43082, USA

Dr. N. Yaacoub, Dr. J.-M. Grenèche
IMMM
UMR CNRS-6283
Université du Maine
Avenue Olivier Messiaen, 72085 Le Mans cedex, France

Prof. R. Valenzuela
IIM
Universidad Nacional Autónoma de México
Circuito Exterior
Ciudad Universitaria
Coyoacán 04510, Mexico

DOI: 10.1002/ppsc.201800104

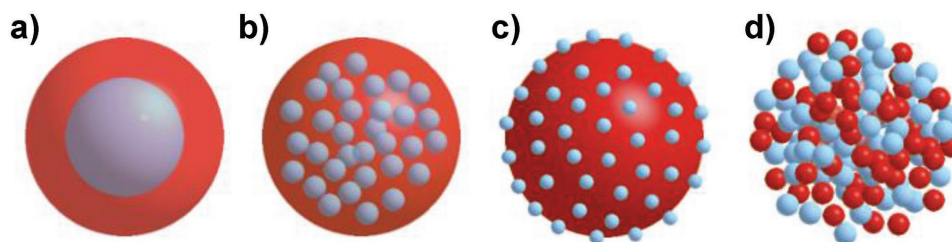


Figure 1. Schematic description of the main isotropic in shape granular hetero-nanostructures usually reported in the relevant literature: a) core-shell, b) embedded, c) raspberry-like, and d) heterocoagulate or nanoaggregates.

deposit is avoided, or at least controlled, in favor to its growth on the seed surface. Typically, the strains between the seed and the deposit crystallographic lattices must be as low as possible, to make the energy barrier for a homogeneous nucleation not so small compared to that for a heterogeneous one. Besides, the chemical and physical interfacing of the different materials must induce the lowest interfacial structural defect density, the existence of epitaxial association between the seed and the deposit being the best crystallographic configuration. Then, in order to tune the final morphology of the growing composites, one has to optimize the operating synthesis conditions to define the final morphology. Colloidal chemistry offers such material engineering opportunities.^[4] Among these experimental parameters, the nominal matter content ratio between the seed and the deposit, the introduction temperature of the deposit precursors, or the reaction time have been extensively varied to form more or less isotropic in shape granular hetero-nanostructures. These heterostructures consist mainly of core-shell nano-objects, nanoaggregates, raspberry-like particles, heterocoagulates, or embedded multicores systems (Figure 1).^[2] All of these architectures have of course the advantage of exhibiting large interfacial surfaces but they have also the richness of responding differently to an external chemical and/or physical stimulus (magnetic, electric, optic, etc.).^[3]

In this context, we were interested in using colloidal chemistry in order to prepare one of the most important classes of magnetic granular nanomaterials, the exchange-biased (EB) one. This class consists of a proper combination of two different magnetically ordered materials, for example, ferro- or ferrimagnetic (F) and antiferromagnetic (AF), through textured hetero-nanostructures. This combination gives rise to the EB effect, which is correlated to the magnetic coupling between the common interface shared by the F and AF phases, when it is cooled through the Néel temperature T_N of the AF component under an applied high magnetic field. EB feature usually leads to a shift along the magnetic field axis and an increase in coercivity of the hysteresis loop.^[5] In most of the cases, the largest fraction of remnant magnetization is given by the F component and the role of the AF constituent is to keep the moment in a fixed direction.

There are now thousands of reports on the production of F NPs coated by an AF shell in a core-shell-like structure,^[6] or inversely, AF NPs coated by a F shell.^[7] Seed-mediated growth in a liquid solution is the most employed route to produce such nanostructures, regarding its capability to ensure epitaxial growth, which is one of the requirements for EB coupling. Nanoaggregates, in which F and AF nanocrystals are intimately

mixed, are also widely described. They are very often prepared using high energy mechanosynthesis including mechanical milling or alloying under controlled atmospheres.^[8] F cores embedded in an AF matrix leading to the so-called embedded multicores morphology are also subject of intense researches. Such composites are mainly prepared by physical vapor deposition^[9] since these routes allow a well-controlled microstructure (in terms of core size, size distribution, and core-core distance) in the final systems. To the best of our knowledge, there are no reports on the production of core-shell, aggregate, and embedded morphologies by means of the same material processing route. The valuable route for the preparation of a certain morphology is often less adapted for the preparation of another. In the same time, it is well established that the synthesis conditions have a strong impact on chemical and physical properties of the prepared objects, including their EB feature, making the investigation of the morphology effect on EB not easy at all to be achieved. Only a single synthesis route suitable for all the morphologies may allow such kind of study. So in this context, using seed-mediated growth in polyol medium, we decided to produce all these morphologies, with respect to perfect epitaxial interfaces for EB feature, and to study how these architectures may impact EB. So we focused our study on the Fe_3O_4 -CoO magnetically contrasted system. The cobalt monoxide (CO) crystallizes in the rock salt structure. It consists of an fcc oxygen lattice, in which all the octahedral sites are occupied by cobalt cations. Magnetite is an iron oxide (IO). It crystallizes in the inverse spinel structure, which also consists of an fcc oxygen lattice whom the half of the octahedral sites (B sites) and the eighth of the tetrahedral ones (A sites) are occupied by iron cations. The spinel unit cell is almost twice that of the rock salt (0.8396 nm vs 0.4262 nm), in such a way that the misfit between corresponding interplanar distances remains very small (for instance, d_{111} and d_{222} distances for the rock salt and spinel structures are of 0.24604 and 0.24237 nm, respectively), making feasible the epitaxial growth of one on the surface of the other. IO is ferrimagnetic with a Curie temperature (T_C) of 850 K. CO is antiferromagnetic with a T_N of 298 K, close to the room temperature, making experimental EB evidence easy to achieve. For these reasons, this system was the subject of intense research in the form of multilayers.^[10] Interestingly, a few works have been reported on this system in its granular form. They are scarce and most of them focus on core-shell particles.^[6a,b]

In this report, 10 nm sized F IO NPs were synthesized by forced hydrolysis of iron acetate in a polyol^[11] and then used as seeds for AF CO nanocrystals growth. This crystallochemical step is carried out by dispersing the preformed seeds, washed

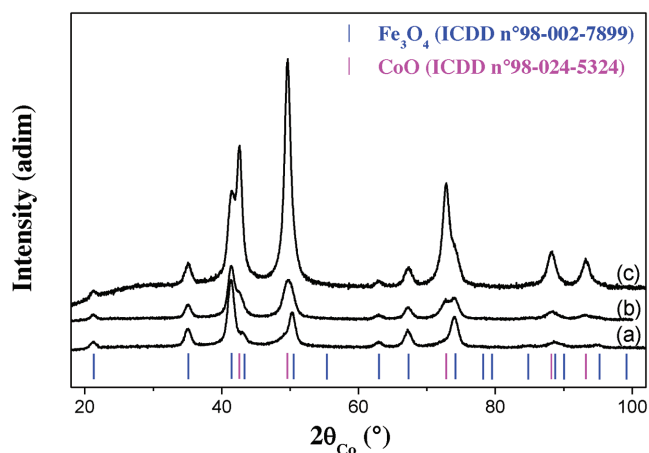


Figure 2. XRD patterns of the as-produced composite powders: a) sample A, b) sample B, and c) sample C.

and dried, in a fresh polyol solution of cobalt precursors. Acting mainly on the iron/cobalt atomic ratio, the morphology of the resulting powders was varied from a core-shell (sample A) to an aggregate (sample B) and an embedded (sample C) architecture. Their structural and magnetic properties were investigated, in regard to their final morphology. Their crystal growth mechanism was also discussed, highlighting the role of the material processing conditions on EB feature.

2. Results and Discussion

2.1. Structure and Microstructure

The X-ray diffraction (XRD) patterns recorded for all the prepared composite powders are reported (Figure 2).

As expected, they correspond to the superposition of the XRD signatures of IO and CO in their spinel (ICDD No. 98-002-7899) and rock salt (ICDD No. 98-024-5324) structures, respectively. The CO peaks' intensity increases proportionally with the quantity of cobalt acetate introduced during the synthesis, in agreement with a consequent increase of the CO content in the resulting composites. In order to confirm this characteristic, X-ray fluorescence spectroscopy (XRF) was performed and the Fe/Co atomic ratio was determined for the three different composites. In practice, it was calculated from

the integration of iron K_{β} and cobalt K_{α} X-ray emission peaks, considering only the oxide phases. The obtained values are presented in Table 1.

The emission bands of these two elements are partially overlapped, thus making their exact quantification hard; despite this difficulty, the IO/CO weight ratio was calculated on the basis of the Fe/Co ratio and the result appears in good agreement with the values inferred from Rietveld analysis of the recorded XRD patterns (Table 1).

The refined lattice constant values of the constitutive phases (Table 1) are in agreement with those of bulk Fe_3O_4 and CoO. In contrast pristine particles, used as seeds, exhibit a lattice parameter slightly smaller than that of Fe_3O_4 . This is attributed to their partial oxidation in air, making their chemical composition closer to that of maghemite $\gamma-Fe_2O_3$ than that of Fe_3O_4 .^[12] The chemical composition evolution of IO in the final composite powders may derive from two different paths. In one, the oxidized seed surface iron cations are reduced into ferrous ones when they are placed in the polyol solvent, before CO deposition. Polyols are known as efficient reductive agents for several transition metal cations^[13] and their ability to change IO composition from maghemite to magnetite can really be effective. In the second path, Co^{2+} ions diffuse during the synthesis toward the cation vacancies formed in the seeds during their oxidation in air, before their dispersion in the CO growth polyol solution. In such a situation, the composition of IO crystals becomes similar to that of $Co_xFe_{3-x}O_4$ solid solution with a lattice parameter close to that of bulk cobalt ferrite, which is itself very close to that of bulk magnetite (8.3940 vs 8.3900 Å, from ICDD Nos. 98-010-9044 and 98-002-7899, respectively).

Mössbauer spectrometry was then performed on the composite powders, in order to determine more precisely the structure of IO. The spectra collected at 300 K (Figure 3) are composed of sextets with broad and asymmetric lines, while a doublet with broadening lines was observed for the pristine IO powder. The composites' spectra were adjusted by superposition of a principal sextet and a minor doublet. The sextet is linked to the ferrimagnetic state while the doublet depends on the superparamagnetic one. One may claim that the spinel NPs are mostly in a blocked state at 300 K in all the prepared composites, due to the increase of their whole magnetic anisotropy, probably derived from the presence of an effective exchange anisotropy instauration. The broadening of the sextet lines was observed for all the composite samples. The asymmetric appearance depends on the presence of different combined

Table 1. Main structural and microstructural properties of the produced composites as inferred from XRD and XRF analysis, compared to those of pristine iron and cobalt oxide prepared separately as references.

	XRD							XRF		
	$a(\text{IO})$ Å ± 0.005	$a(\text{CO})$ Å ± 0.005	$[\text{IO}]/[\text{IO}+\text{CO}]$ wt% ± 10	$\langle \text{spinel}_{\text{LXRD}} \rangle$ nm ± 1	$\langle \text{rocksalt}_{\text{LXRD}} \rangle$ nm ± 1	$\langle \text{spinel}_{\text{c}} \rangle$ [%]	$\langle \text{rocksalt}_{\text{c}} \rangle$ [%]	Fe at% ± 2	Co at% ± 2	$[\text{IO}]/[\text{IO}+\text{CO}]$ wt% ± 2
IO	8.378	–	–	10	–	0.09	–	100	0	–
CO	–	4.259	–	–	12	–	0.13	0	100	–
Sample A	8.409	4.267	71	16	8	0.3	1.1	62	38	63
Sample B	8.401	4.269	54	16	10	0.4	0.4	56	44	57
Sample C	8.405	4.268	27	17	14	0.6	0.2	24	76	25

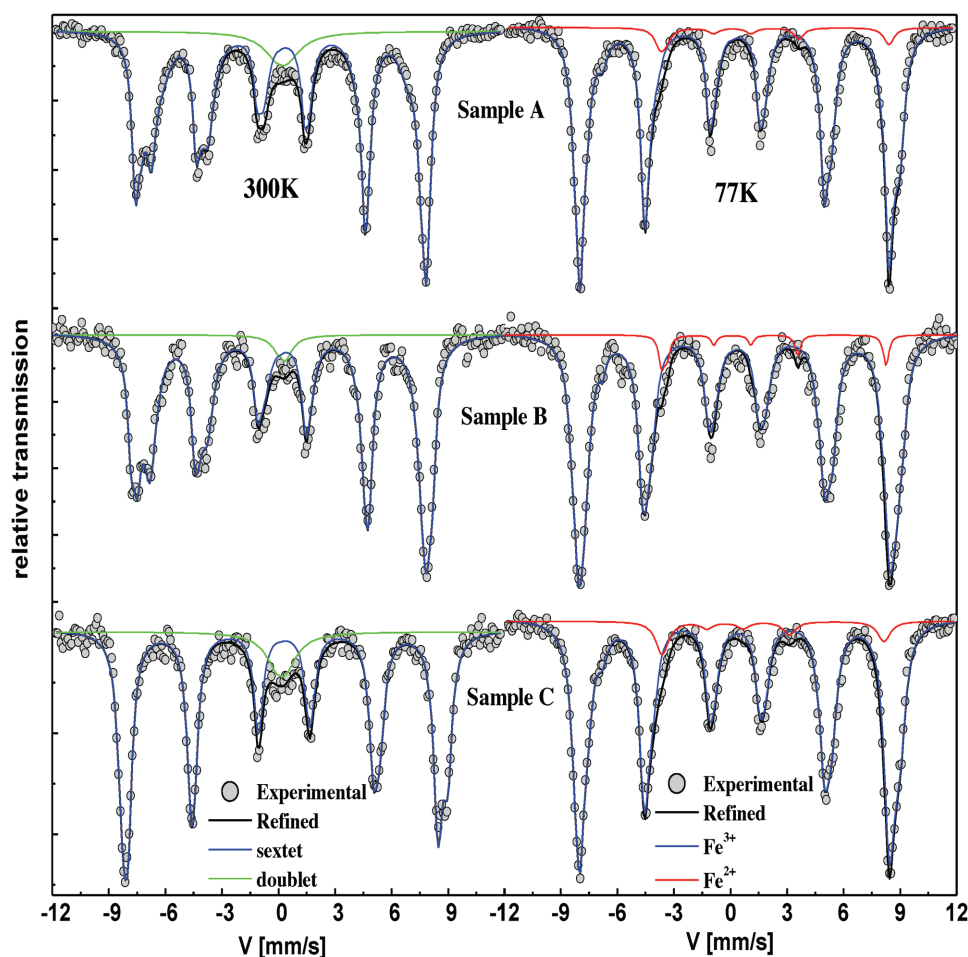


Figure 3. 300 K (left side) and 77 K (right side) Mössbauer spectra of the as-produced composite powders (black scatters) superposed to the refined ones (continuous black line).

sextets, belonging to Fe^{2+} and Fe^{3+} cations occupying the A and/or B sites of the spinel lattice.

The Mössbauer spectra recorded at 77 K (Figure 3) contributed to a complementary observation. They appeared to be constituted by only the sextets contribution, always with large lines' width, thus confirming that all the magnetic core particles are in a blocked state at this temperature. This broadening can also be the signature of a chemical heterogeneity of the spinel phase.^[14] The spectra were successfully refined considering three components: two for the Fe^{3+} ions in the sites A and B, one for the Fe^{2+} ions in the B sites. The mean values of the isomer shift δ , the hyperfine field B_{hyp} , and those of the quadrupole splitting 2ϵ associated to all the species are listed in Table 2. The hyperfine field linked to the Fe^{2+} ions is very

similar to the value usually found for magnetite^[15] for all the three composite samples. The value associated with Fe^{3+} ions in the A and B sites, in contrast, was found larger than that for pure magnetite,^[16] and smaller than that for CoFe_2O_4 .^[17] Moreover, the observed ferrous ions' atomic ratio in composites is about 8%, lower than the expected 33% for pure magnetite, suggesting the diffusion of Co^{2+} ions in IO lattice during CO growth, replacing progressively in the spinel B sites, Fe^{3+} vacancies^[12] and leading a decreasing Co^{2+} gradient concentration, from their surface to the inner core of IO seeds. This concentration gradient is consistent with a final chemical composition of $\text{Co}_x\text{Fe}_{3-x}\text{O}_4\text{-CoO}$ instead of $\text{Fe}_3\text{O}_4\text{-CoO}$. It creates chemical heterogeneity in the spinel cores but in the same time, it favors a kind of chemical continuity between

Table 2. Refined values of hyperfine parameters inferred from the composite spectra recorded at 77 K.

	Fe^{3+}				Fe^{2+}				T(K)
	$\langle\delta\rangle$ mm s ⁻¹ ± 0.01	$\langle 2\epsilon\rangle$ mm s ⁻¹ ± 0.01	$\langle B_{\text{hyp}}\rangle$ T ± 0.5	Ratio at% ± 2	$\langle\delta\rangle$ mm s ⁻¹ ± 0.01	$\langle 2\epsilon\rangle$ mm s ⁻¹ ± 0.01	$\langle B_{\text{hyp}}\rangle$ T ± 0.5	Ratio at% ± 2	
Sample A	0.54	-0.03	51.1	91	1.15	2.00	36.7	7	77
Sample B	0.50	0.06	51.3	92	1.05	2.50	35.5	8	77
Sample C	0.52	0.02	51.0	93	1.16	2.50	36.1	7	77

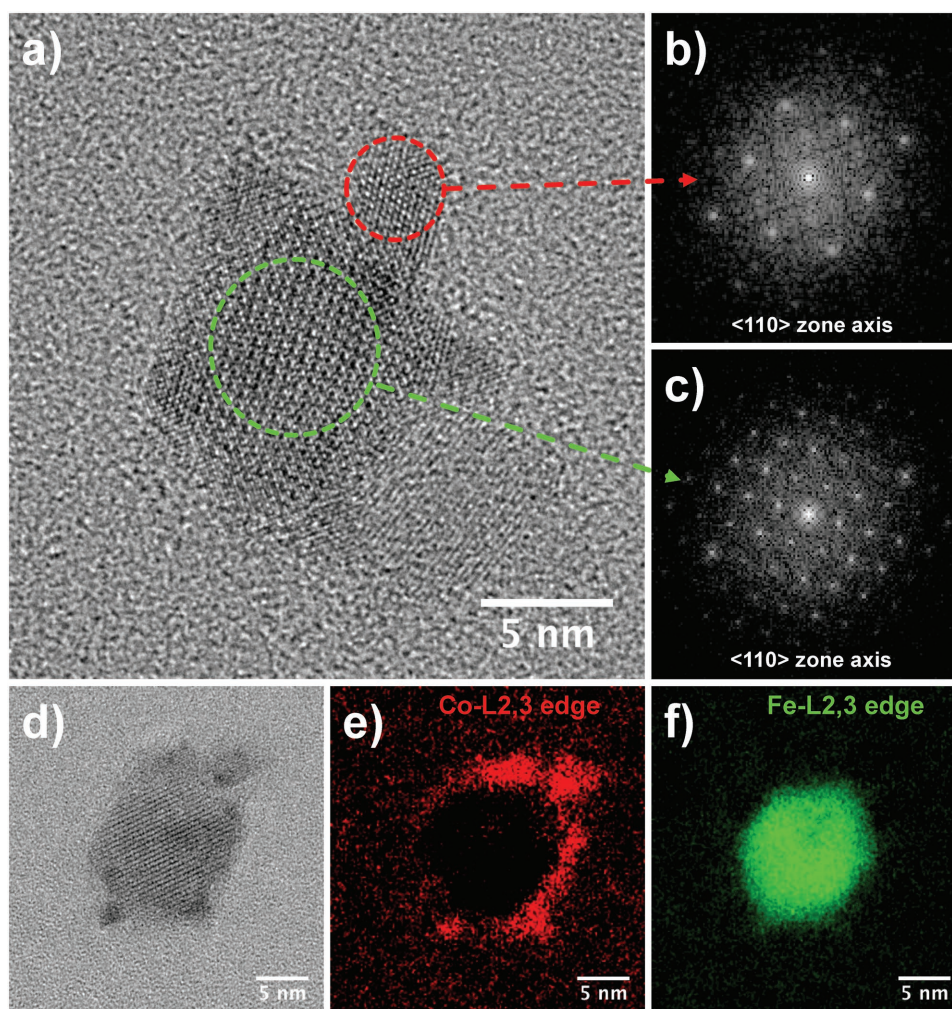


Figure 4. TEM analysis of sample A: a) HRTEM image of a core-shell particles, b,c) FFT patterns of two representative crystallographic areas constituting such an aggregate: b) related to a CoO *Pmm* cubic phase and c) corresponding to the Fe₃O₄ *Fdm* cubic phase, d) HRTEM and e,f) EFTEM elemental mapping of a particle, focusing on its Co (in red) and Fe (in green) contents.

the seeds and the deposits, meaning that CO heterogeneous nucleation could be privileged face to a homogeneous one, thus allowing a real material engineering and design of the rising heterostructures.

High-resolution transmission electron microscopy (HRTEM) was thus carried out on all the prepared samples to confirm the effective formation of the desired hetero-nanostructures in which both spinel and rock salt crystals share common faces. The collected images are given in **Figures 4–6**.

First of all, they illustrate the high-crystalline quality of all the produced constructs, since continuous atomic plans can be observed in all the observed particles sections. Second, they evidence clearly two different crystal populations: one with an average diameter of 10 nm and a fast Fourier transform (FFT) associated with a 8.4 Å unit cell parameter with a *Fdm* space group, and another one with a mean diameter much smaller and an FFT related to a 4.2 Å unit cell parameter of a rock salt lattice (*Fmm* space group). Third, the comparison between the three different composites shows that the lower their CO content, the more the particles are organized in individualized

forms. The small CO particles (about 3 nm) tend to surround the Co_xFe_{3-x}O₄ bigger ones (sample A typically). As CO content increases, its crystal size increases (to about 5 nm) forming progressively a continuous matrix enclosing the 10 nm sized Co_xFe_{3-x}O₄ ones (sample C typically). The chemical mapping, performed energy filtered transmission electron microscopy (EFTEM) or scanning TEM (STEM)-X-ray energy-dispersive spectroscopy (XEDS) imaging confirmed this morphology evolution from sample A to sample C.

It is also important to underline that, in each case, the two phases share the same crystalline axis; in other words, CO phase grows in an epitaxial way on the IO-based one. This epitaxy is a key issue for CO heterogeneous nucleation and a promoting factor for seed-mediated growth in the polyol reaction solution. Experimentally, it can be correlated to the large average crystal size inferred from XRD analysis for each phases, the so-called XRD crystal size being in fact the average coherent crystallographic length.^[12,18,19] Fourth, for all the explored samples, there are no evidences of any structural defects, like dislocations, stacking faults, or surface amorphization.

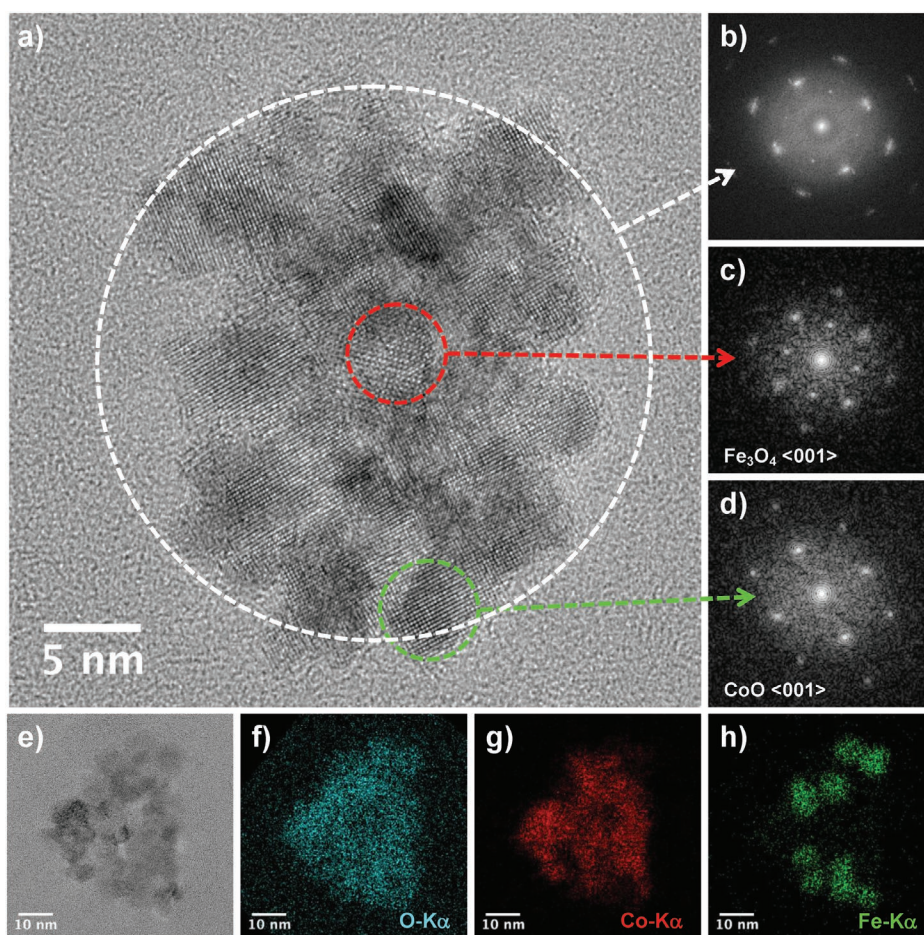


Figure 5. TEM analysis of sample B: a) HRTEM image of a nanoaggregate, b–d) FFT patterns of three representative crystallographic areas of the aggregate, and f–h) STEM-XEDS chemical mapping of an aggregate, focusing on its O (in cyan), Co (in red), and Fe (in green) contents.

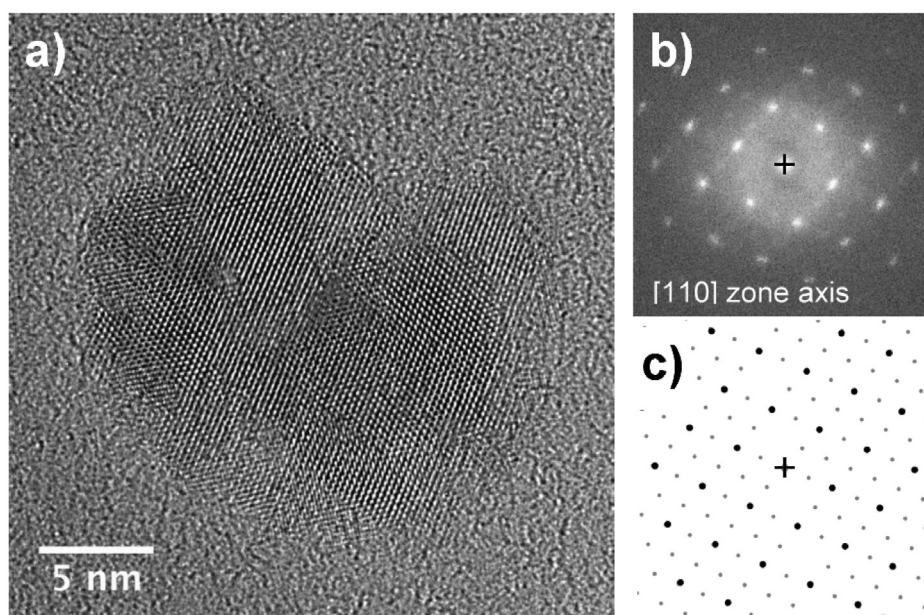


Figure 6. TEM analysis of sample C: a) HRTEM image of a multicore embedded particle, b) FFT pattern of all the representative crystallographic area constituting the particle: strong and weak reflections are related, respectively, to CoO and iron-based oxide. c) Calculated SAED, CoO: black dots and iron-based oxide: small gray dots.

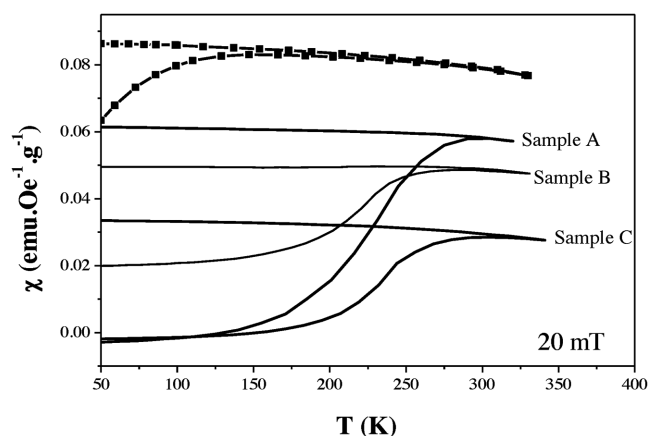


Figure 7. FC and ZFC thermal variations of the magnetic dc susceptibility of pristine IO (scatters) and composite NPs (continuous line), measured at 20 mT.

2.2. Magnetic Properties

The three different types of composite were finally characterized from the magnetic point of view, in order to check the influence of their morphology on their magnetic properties. The thermal variation of their magnetic susceptibility $\chi(T)$ was measured in field-cooling (FC) and zero-field-cooling (ZFC) mode for an applied dc magnetic field of 20 mT and compared to that of bare IO (Figure 7).

As expected, the whole samples exhibit a superparamagnetic behavior at room temperature with a blocking temperature, T_B , defined at the maximum point of the ZFC branch, which increases when the CO content increases. This increment is much more important between bare IO and the composites than between the composites themselves. Typically, T_B is displaced from 155 K to values close to 300 K. This result agrees well with that inferred from Mössbauer spectrometry analysis and suggests once again that the magnetic anisotropy of the ferrimagnetic spinel crystals increases significantly when they are coated by the antiferromagnetic rock salt ones. In other words, this feature is observed when EB is installed.^[5,6]

Two other contributions to T_B increment must be highlighted. First, the Co^{2+} diffusion into the spinel lattice may lead to an enhancement of the core's magnetocrystalline anisotropy constant. Second, when the magnetic cores are progressively distanced by CO AF nanocrystals, the dipolar interactions weaken and the average T_B value proportionally decreases. We can state that the dipolar interactions contribution to T_B increment is negligible if

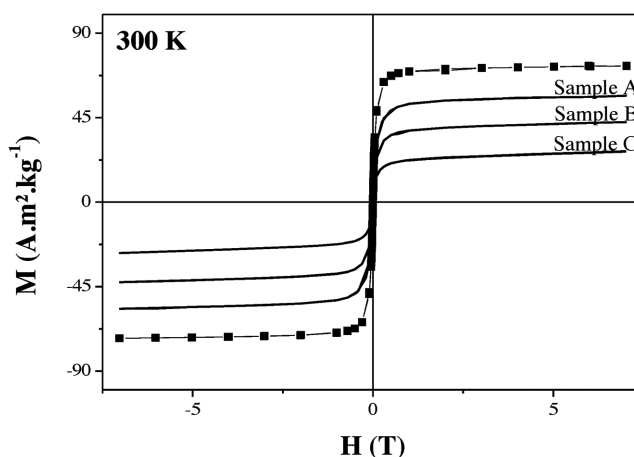


Figure 8. $M(H)$ loops recorded at 300 K on the as-produced composite NPs (continuous line) and compared to that of pristine IO NPs (scatters).

compared to EB and magnetocrystalline contributions. The small variation on T_B value in the 288–304 K range between samples A, B, and C (Table 3), which is assumed to be mainly due to a change in the dipolar interaction strength, is a good illustration about that. The $M(H)$ loops of the composites were also recorded at 300 K and compared to that of pristine IO NPs (Figure 8). They exhibit a slight remanence and coercivity while that of pristine IO does not. These features agree with the observed evolution on T_B average value, and are assumed to be mainly due to the magnetocrystalline anisotropy increase of the F cores, EB being less effective at this temperature (close to CO T_N value).

Finally, to complete the magnetic characterization of the produced samples, their $M(H)$ loops were recorded at 5 K, namely, below their T_B temperature. They were plotted in both ZFC and FC modes in Figure 9 (left side), the FC corresponding to cooling from 330 K (far from CO T_N value) to 5 K under an applied cooling field of 7 T.

As expected, open hysteresis loops, with characteristic remanence and coercive field of hard magnets, were obtained for all the composite samples. Coercive field values as large as 1 T were measured. In contrast, their high field total magnetization is reduced by CO content, which behaves as a diluting agent as far as it does not provide a net magnetization. Interestingly, a net left shift of the FC loops, as compared with the ZFC ones, along the field axis was systematically observed for these samples, evidencing EB. The exchange field H_E that usually measures the FC loop horizontal shift was found to be of the order of hundred mT, its largest value being reached in the core-shell composite NPs.

Table 3. Main magnetic characteristics measured on the as-produced composite and seed powders compared to those obtained on the same powders largely diluted in diamagnetic alumina (4.2 wt%) to reduce significantly dipolar interaction effects.

	As-produced powders				Diluted in alumina powders				
	T_B (20 mT) K	H_C (ZFC, 5 K) T	H_C (FC, 5 K, 7 T) T	H_E (5 K, 7 T) mT	M (5 K, 7 T) [A m ² kg ⁻¹]	H_C (ZFC, 5 K) T	H_C (FC, 5 K, 7 T) T	H_E (5 K, 7 T) mT	M (5 K, 7 T) [A m ² kg ⁻¹]
IO	155	0.03	0.03	0	83.0			0	84.0
Sample A	298	0.97	1.14	170	72.0	1.14	1.18	50	74.0
Sample B	285	0.19	0.30	120	49.0	0.84	0.91	93	60.0
Sample C	304	0.86	0.89	81	27.0	0.87	0.99	125	38.0

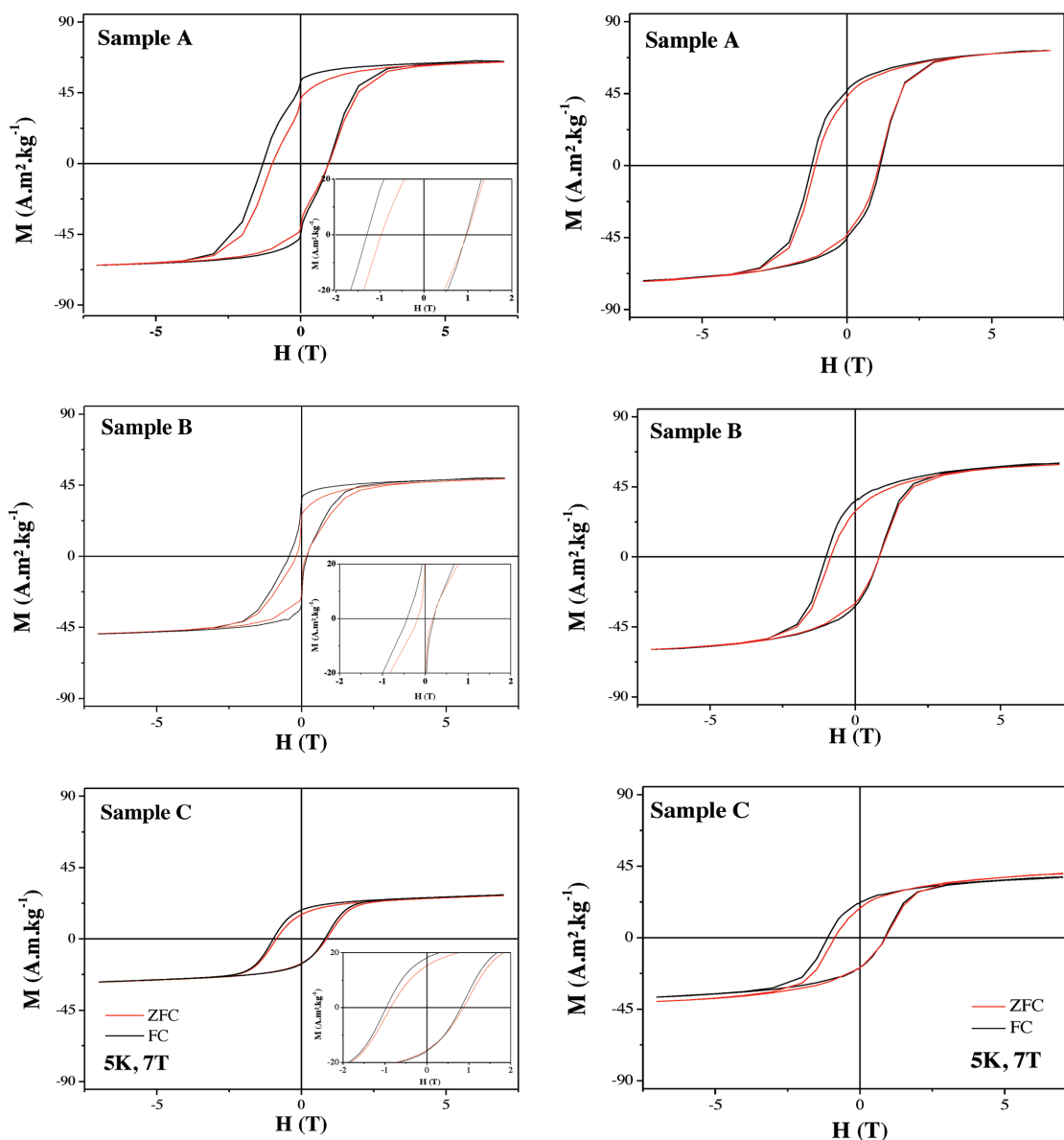


Figure 9. $M(H)$ loops recorded at low temperature (5 K) on the as-produced composite powders (left side) and 4.8 wt% diluted in diamagnetic alumina (right side), in FC (applied cooling field of 7 T) and ZFC modes. Dilution was aimed to reduce dipolar interactions between F cores.

The composites coercive field in ZFC hysteresis loops is significantly larger than that of bare IO. However, the difference is not as large as could be expected as a consequence of the EB effect. This apparent increase in magnetic anisotropy in the spinel core is ascribed to the Co^{2+} ions diffusion into the F lattice. The magnetic properties of the prepared nanocomposites can be better understood considering the two different contributions: the exchange anisotropy coupling at F–AF crystals interface, and the enhancement of the magnetocrystalline anisotropy in the F cores. The 5 K hysteresis loops in Figure 9 exhibit an additional feature in the low applied field region. As H approaches 0, magnetization decreases faster with a sharp change of slope. This effect can occur by a physical rotation of the magnetic particles during the field reversal, or as a result of dipolar interactions that reinforce cooperative magnetization reversal in the small

field range. It must be highlighted that the amplitude of slope's variation depends on CO content. It is more significant for the nanoaggregate morphology, small for the core–shell and unnoticed for the embedded one. This direct correlation between CO content and extent of slope's rate suggests the dependence from F cores' dipolar interactions, the richest composite with its embedded morphology being completely unfavorable for dipolar interactions. In order to investigate the origin of this hysteresis loops' singularity around $H = 0$, all the composite powders were diluted in a diamagnetic matrix of alumina (Al_2O_3) and characterized from the magnetic point of view. The dilution is aimed to separate the particles constituting the composite powders, thus weakening dipolar interactions' effect on total magnetization. Different dilution ratios were studied; here, we report just the highest dilution ratio results, with 4.8 wt% powder in Al_2O_3

(Table 3). Again, hysteresis loops were recorded at 5 K; FC loops were cooled from 330 K under 7 T applied field. The results in Figure 9 (right side) show that the singularity at $H = 0$ completely disappears for the considered dilution ratio, which is high enough to weaken dipolar interactions' effect between NPs. Other effects of dilution are the increase of coercive field, remanence, and saturation magnetization, coherent with dipolar interactions' weakening, and, unexpectedly a decrease of exchange field. The described effects are stronger in the nanoaggregate composite type, as evidenced in Table 3. Focusing now on the data inferred from these last plots, the remnant magnetization values of all the composite samples were found to be different for the positive and the negative branches of FC cycles; in the positive branch its value is about the 60% of the magnetization at 7 T (taken as saturation magnetization), while it approaches 50% in the negative one. Typical remanence values for bulk spinel ferrites are lower or equal to 50% saturation magnetization, because of their cubic magnetocrystalline anisotropy, while magnetic materials with uniaxial symmetry commonly report ratios higher than 50%. We can thus think that exchange anisotropy, which has a uniaxial symmetry type, appears in the samples by increasing the remanence value in the FC measurements.

The core-shell composite NPs exhibit the highest value of coercivity and remanence, the highest magnetization of course, but it shows the lowest exchange field H_E when diluted in Al_2O_3 . In contrast, it was found to have the highest H_E in the case of as-produced powder. These results underline the complex relation between dipolar interactions and exchange anisotropy phenomenon, but still reinforce the hypothesis that the core-shell design is the most favorable to achieve exchange biased nanostructured hard magnets.

In conclusion, the magnetic characterization of our samples allowed understanding their overall magnetic behavior that was found to be a compromise between three different mechanisms that are dipolar interactions, exchange anisotropy at the F/AF phase interface, and magnetocrystalline anisotropy increment in F cores thanks to Co^{2+} diffusion into their crystalline lattice. The achievement of these mechanisms is directly related to the crystal growth conditions of the studied composites. The size of the F and AF crystals, their epitaxial crystallographic relationship, the final chemical heterogeneity of the seeds, and the deposit content contributed to design functional nano-objects with hard magnetic properties.

Such trends were confirmed by the low-temperature first-order reversal curves (FORC) measurements on composite powders of sample A and sample C that are, respectively, the one with the higher and the lower AF ratio in their composition. FORC measurements were not attempted for seed powder, since pristine IO nanoparticles are magnetically soft, that is, anhysteretic, and therefore not relevant for FORC investigation. FORC is particularly well adapted to the characterization of magnetic anisotropy and interactions.^[20] They also represent a useful experimental method for investigating dipolar effects, particularly as a function of the microstructural characteristics (aggregation state, average crystal size, phase ratio, etc.). The recorded 120 K $M(H)$ and FORC curves on as-produced sample A, sample C, and diluted in alumina sample A (not shown here) are used to plot the 2D FORC diagrams, which report the coercive field distribution on their horizontal axis and the interaction field distribution on their vertical axis (Figure 10). As a first lecture, the obtained diagrams are consistent with a dispersed collection

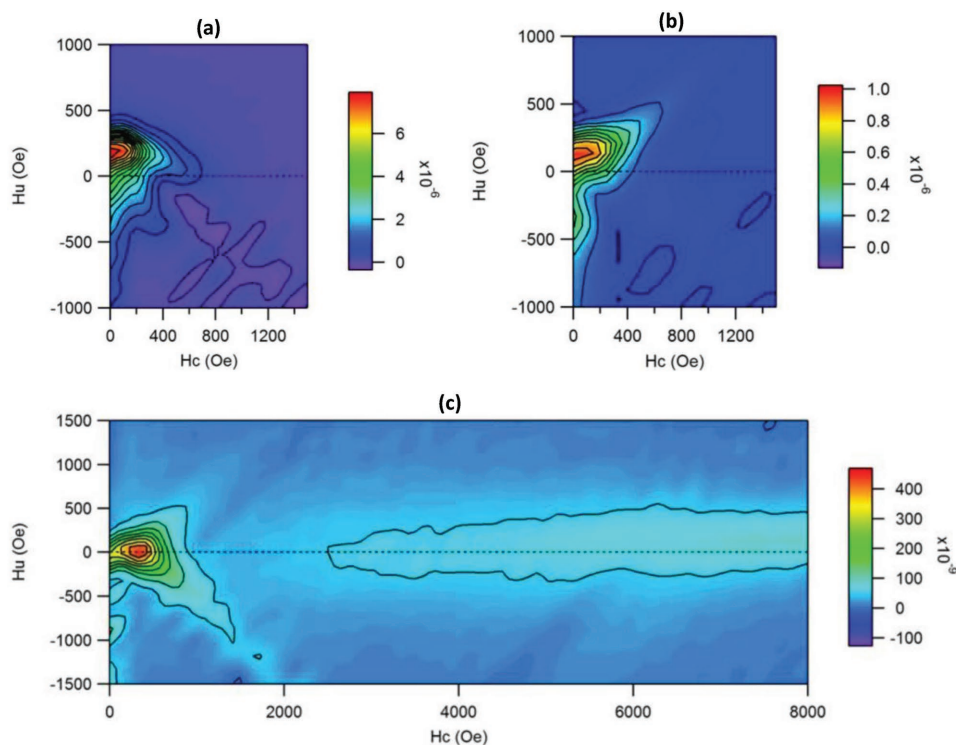


Figure 10. Low-temperature (120 K) FORC diagrams recorded on the as-produced a) sample A, b) sample C, and c) sample A diluted in alumina.

of pseudo-single-domain (PSD) particles that are more or less interacting, depending on their intimate morphology. They exhibit a maximum that is centered at a switching field (H_c : horizontal axis) that correlates with the coercivity of the sample, and an interacting field (H_u : vertical axis) that correlates with the type of interaction (dipolar vs exchange interaction) between its constituting F crystals. In the present case, focusing on the as-produced powders, the FORC diagrams are consistent with a dispersed collection of PSD particles that are interacting more strongly in sample A than in sample C.

In fact, the FORC diagram has a peak that is more shifted toward positive values of H_u in the case of sample A than in sample C (Figure 10a,b). Usually, a peak shift toward positive H_u values suggests that the dipolar interactions are strong, while a shifting toward negative values refers to the existence of exchange interactions between the magnetic particles. Interestingly, after diluting sample A in a large amount of diamagnetic alumina (4.8 wt% of sample A on the total mass), the recorded FORC diagram (Figure 10c) displays a peak's shift that is even smaller than the one of sample C, confirming that after dilution the ferrimagnetic cores are completely separated and that interaction between them are weak. As expected, in sample A the F cores interact in a bigger extent because this is the sample with the lower AF content; also if the AF shell surrounds each F core, its thickness is not high enough to completely avoid the dipolar interactions. In the case of sample C, the F cores are embedded in an AF matrix and are more spaced to each other; this morphology brings to a lower extent of the dipolar interactions effect.

2.3. Crystal Growth

The formation of nanoparticles in a solution involves a series of complicated processes including chemical reactions, nucleation, growth, and precipitation. Each process is affected by many experimental variables and it is much more tedious when seed-mediated growth is occurring. The fabrication of granular heterostructures means the capability to produce the largest interfacial surfaces. Ideally, it also means the possibility to tune the operating synthesis conditions in favor of an epitaxial growth of the deposits on the seeds, which is a fundamental requirement in building efficient exchange-biased nanostructured magnets.

Besides, a minimal thickness of AF deposit is required for EB evidence. In the same time, it must remain thin enough to limit the total magnetization decrease, which is a drawback for most magnetic-based applications. Simultaneously, increasing this thickness contributes to reduce dipolar interaction strengths. So varying the morphologies from core-shell to embedded multicores allows acting on this thickness. Finally, embedded architecture reduces significantly dipolar interactions and avoids the installation of any collective magnetic glass state, with lower magnetization and coercivity, between frustrated and frozen macrospin F cores. The core-core distances are the largest in this geometrical configuration by comparison to the two others. In contrast, the nanoaggregate morphology exhibits an opposite configuration. The probability to find two adjacent cores is the highest and

the ratio of common AF/F interfaces compared to the total exposed F surfaces is the smallest. As a consequence, the dipolar interactions are the strongest and the EB feature is the weakest. Finally, the core-shell arrangements offer the best compromise, since all the F cores are distant by at least two AF shell thicknesses.

Colloidal chemistry clearly appears as a powerful material engineering route to produce functional magnetic nanostructures in which dipolar interactions may be easily tailored.

Focusing on material engineering, the production of nanocomposites by seed-mediated growth in a solution involves dynamical thermodynamic and kinetic processes. Transport of atom-size matter to the surface, surface restructuring, and detachment/reattachment are all occurring in the reaction liquid medium. We believe that in the present situation, the fact that dissolved Co^{2+} cations start first by filling the spinel octahedral cation vacancies into the dispersed seeds, before CO formation, promotes the nucleation of this phase at the surface of the seeds. The polycrystalline character of CO in the core-shell nanoparticles suggests that discrete CoO nuclei are formed on $\text{Co}_x\text{Fe}_{3-x}\text{O}_4$ crystal face surfaces. These nuclei grow first through diffusion from the solution and restructuring on the seed surface, to reach at the end a continuous shell of about 1 nm in thickness, covering all the seed volume (see ref. [6a]). Note that too fast diffusional transport of matter onto surface, as compared to the restructuring processes, would lead to fractal growth.^[21] In contrast, too slow transport would result in the overall shape equilibration by restructuring processes, leading to thermal-equilibrium Wulff shapes.^[22] Finally, comparable time scales between the two phenomena would favor well-defined nanocrystal shapes during nanoparticles growth.^[23] The fact that the diffusion proceeds here in a liquid phase supposes that this feature is fast, but the fact that all our HRTEM observations do not evidence any fractal morphology suggests that it is not so fast compared to the on-surface and detachment/reattachment processes. In the present situation, the most probable scenario is that both phenomena have comparable time scales and contribute almost equally in CoO growth, leading to a well shape-defined core-shell pseudo-single crystal (as illustrated in Figure 4a) for weak CO content (sample A).

For the extreme opposite operating conditions, namely, for high CO content (sample C) a multicore embedded morphology is obtained. The microstructural proximity of the CO matrix in this type of composite with that of bare CoO particles (see Experimental Section) suggests that CoO crystal growth proceeds in almost the same way. The very high Co^{2+} precursor concentration in the solution does not exclude both heterogeneous and homogeneous CoO nucleation. The whole formed CoO crystals start growing by diffusion, leading to a final crystal size of 5 nm, like in bare CoO NPs (Figure 11), they then coalesce through oriented aggregation mechanism^[24a] leading to large pseudo-single crystals with typical single-crystal-like diffraction patterns (see Figures 6 and 11). It stands to reason that the driving force for crystal aggregation is the amount of Co^{2+} cations available in the reaction solution. The core-shell morphology is favored by the lower amount of CoO precursor in solution, which remains low enough to prevent the composite particles aggregation.

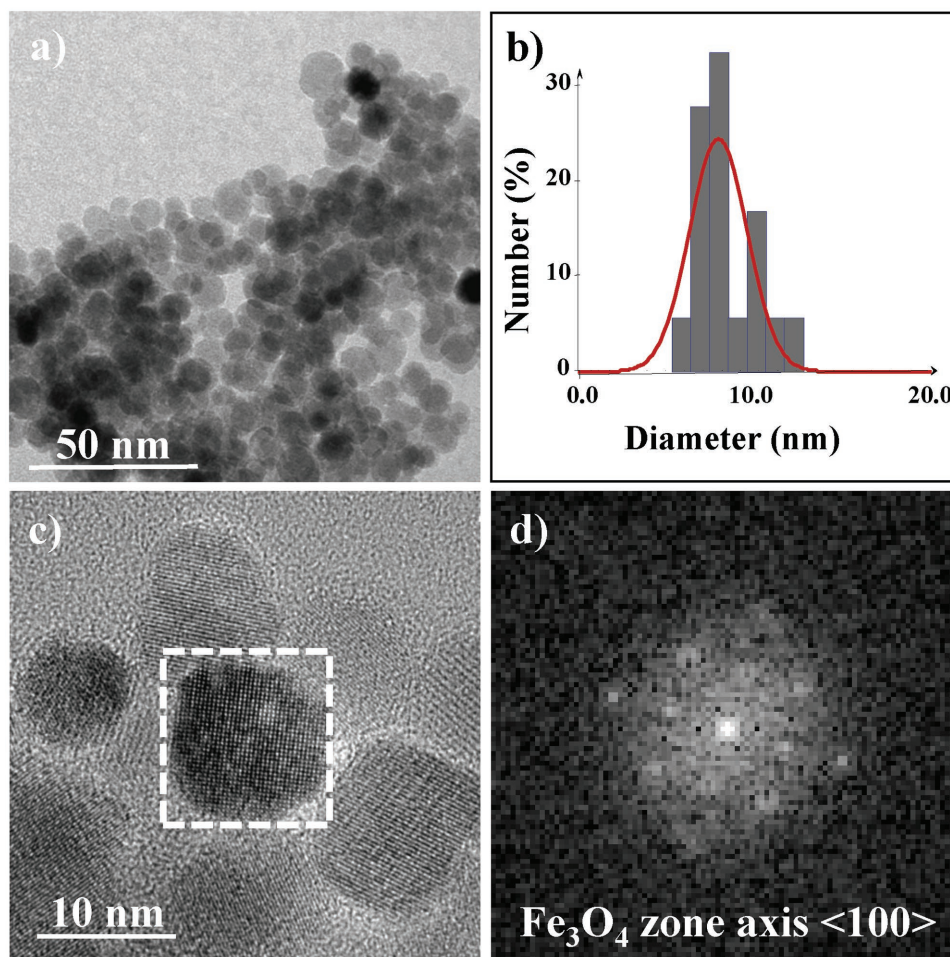


Figure 11. TEM image of an assembly of 10 nm sized polyol-made iron oxide particles, their size distribution and one representative HRTEM image with the FFT pattern calculated for the selected area.

In the case of free CoO, ab initio modeling allows to conclude that polyol molecules are adsorbed at the top of cobalt surface atoms of 5 nm sized CoO cubic nanocrystals. The adsorption does not involve the whole polyol molecule but only its extreme oxygen atoms, the main molecule chains being outside the crystal surface. These chains interact between themselves from one crystal surface to another, allowing oriented crystal aggregation.^[24b] The calculation has also shown that CoO primary nanocrystals exhibit a very low surface energy, 0.8 J m^{-2} , increasing their catalytic capability,^[24b] which may favor the decomposition of the adsorbed organic, leading to the production of CoO pseudo-single crystals.

Table 4. Main processing conditions used for the production of the desired granular hetero-nanostructures in polyol. The expected weight ratio between the seed and deposit phases is indicated.

	C [mmol]	V [mL]	[IO]/[IO+CO] [wt%]
Core-shell (Sample A)	12.5	0.9	75
Nanoaggregates (Sample B)	25.0	1.8	50
Embedded multicores (Sample C)	50.0	3.6	25

3. Conclusion

Magnetically coupled Fe_{3-x}O₄-CoO oxide-based granular heterostructures were successfully synthesized into different morphologies by a seed-mediated growth in polyol medium. This method allows the engineering of core-shell, nanoaggregate embedded configurations by controlling the synthesis parameters, especially the nominal deposit/seed weight ratio. We demonstrated that the complexity in magnetic properties of these materials could be understood in terms of the interplay between exchange-bias coupling, dipolar interaction, and enhancement of magnetocrystalline anisotropy on the spinel cores.

4. Experimental Section

Seed and Composite Powder Preparation: Chemicals: Metal salts Co(CH₃COO)₂·4H₂O and Fe(CH₃COO)₂ and diethylene glycol solvent (DEG, b.p. = 245 °C) were purchased from ACROS. All the products were used without any further purification.

Synthesis: Iron oxide seeds were prepared by forced hydrolysis in polyol medium.^[9] Generally, 23.0 mmol (4.05 g) of anhydrous iron acetate were dissolved in 250 mL of DEG under mechanical stirring and heated under reflux until boiling point (225 °C). NPs were then recovered

by centrifugation, washed with acetone, and dried in air overnight. They are well crystallized, almost uniform in size, and isotropic in shape with an average diameter of 10 nm (Figure 11).

2.15 g (12.2 mmol) of the as-produced seeds were dispersed in a fresh DEG solution of tetrahydrate cobalt acetate of a given content (C), after adding an appropriate amount of distilled water (V) to grow the CoO phase. C and V were varied to tune the final morphology of the produced hybrids, while the hydrolysis ratio h defined as the molar ratio of water on cobalt cation, was almost maintained at 4 (Table 4). In all the cases, the reaction medium underwent sonication at room temperature for 10 min, then heated up to 180 °C, for 18 h under mechanical stirring. The temperature was not increased more to avoid cobalt reduction and metal precipitation.^[25] Cooled suspensions were centrifuged, washed with acetone, and dried in air overnight.

Cobalt monoxide nanocrystals were produced separately by forced hydrolysis in polyol, in the same conditions than those described previously for CO growth on IO seeds, to serve as reference. Typically, 3.11 g (41.5 mmol) of tetrahydrate cobalt acetate and 2.99 mL of distilled water ($h = 4$) were dissolved in 250 mL of DEG and heated up to 180 °C for 18 h under mechanical stirring. NPs were then recovered by centrifugation, washed with acetone, and dried in air. They are polycrystals with specific pseudo-single crystal behavior. They are well-crystallized, almost uniform in size and isotropic in shape with an average diameter of 100 nm, while their constitutive elementary crystals are also isotropic in shape but with a mean size of about 5 nm (Figure 12).

Characterization: Phase Analysis: All the produced powders, pristine IO, CO, and their related composites, were characterized as freshly prepared or stored under vacuum to limit oxidation toward air exposition and overcome criticism on the validity of the collected experimental data.^[18]

Thus, the structure and the microstructure of the powders were analyzed by XRD employing a PANalytical Xpert'Pro diffractometer equipped with a Co K α X-ray source (1.7889 Å). In practice, the patterns were recorded in the 10°–110° 2 θ range (scan step of 0.025 for 2 s) within the θ – θ Bragg–Brentano configuration. Rietveld refinements were then performed using MAUD software.^[26]

The chemical composition was checked by XRF. Typically, a drop of aqueous suspension of each produced powder (20 μ L) was deposited on a clean Prolene membrane and analyzed by using certified solutions with appropriate Fe and Co composition on a PANalytical Epsilon 3XL spectrometer equipped with an Ag X-ray tube operating at 30 kV and 480 μ A current emissions. All XRF spectra were acquired in air for 30 s and analyzed using commercial software provided by PANalytical fabricant.

This analysis was completed by ⁵⁷Fe Mössbauer spectrometry investigations. In practice, ⁵⁷Fe Mössbauer spectra were recorded on all the produced powders, in transmission geometry, using a ⁵⁷Co/Rh γ -rays source. They were acquired at 300 and 77 K in zero magnetic field by means of a conventional constant acceleration transducer and then analyzed by least squares fitting method using Lorentzian functions. The isomer shifts were referred to that of α -Fe at 300 K.

Detailed microstructural analysis was performed thanks to HRTEM observations, carried out on a JEOL 2100F microscope operating at 200 kV. The microscope was equipped with a Schottky emission gun, a high-resolution UHR pole piece, and a Gatan US4000 CCD camera. From the collected images, the particle size distribution was estimated using SAISAM software (Microvision Instruments), calculating the surface-average particle diameter through a statistical analysis obtained by counting about 400 particles considering a spherical particle shape. Besides, chemical elemental mapping was performed using both energy filtered TEM imaging with a Gatan Image Filter GIF 2001 and STEM-XEDS imaging mode thanks to XEDS analyses using a JEOL detector coupled with a scanning TEM device.

Magnetic Analysis: Routine magnetometry was performed using a Quantum Design PPMS magnetometer, working in its VSM configuration. First, the thermal variation curves of ZFC and FC dc susceptibility, χ , were recorded under a magnetic field of 20 mT. The ZFC isothermal magnetization was also recorded at 5 K by cycling the magnetic field H between -7 and $+7$ T. In order to highlight the existence of the EB effect, a measurement of the isothermal magnetization below blocking temperature, after cooling above room temperature, at 7 T field, was also performed. For all the samples, the measurements were performed on the as-produced powders and on their counterparts sufficiently diluted in diamagnetic alumina (4.8 wt%) to avoid dipolar interaction effects. In practice, the as-produced and Al₂O₃ diluted powders were compacted in a diamagnetic plastic tube to prevent physical movement of the grains during the experiments and the collected data were systematically corrected from the diamagnetic contributions. Additionally, FORC measurements were performed on all the produced powders and on the diluted in alumina counterparts. In practice, a saturation field H_{sat} was applied to the sample. The field was then decreased down to a reversal field H_a . The magnetization was measured after measuring moment versus field H_b as the field is swept back to H_{sat} . This process was repeated for many values of H_a , yielding a series of curves. The FORC distribution $\rho(H_a, H_b)$ is the mixed second derivative, that is, $\rho(H_a, H_b) = -\frac{1}{2}\partial^2 M(H_a, H_b)/\partial H_a \partial H_b$. It is plotted as a 2D diagram, in which the coordinates are $H_c = \frac{1}{2}(H_b - H_a)$ and $H_u = \frac{1}{2}(H_b + H_a)$.^[27] A Lake Shore Cryotronics Model 8600 VSM magnetometer was used to measure the

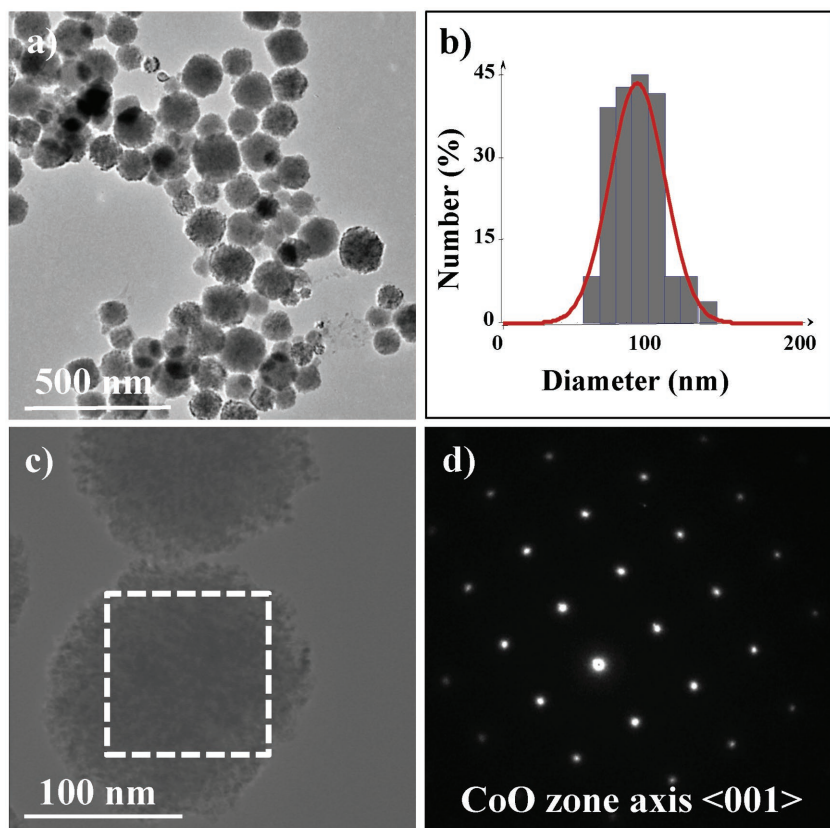


Figure 12. TEM image of an assembly of 100 nm sized polycrystalline and textured polyol-made CoO particles, their size distribution and one representative HRTEM image with the electron diffraction (SAED) pattern recorded for the selected area.

FORCs, and FORCine^[28] was used to calculate the FORC distributions and plot the FORC diagrams.

Supporting Information

Supporting Information is available from the Wiley Online Library or from the author.

Acknowledgements

This work was supported by French Ministry of Research and National Centre for Scientific Research. ANR (Agence Nationale de la Recherche) and CGI (Commissariat à l'Investissement d'Avenir) are gratefully acknowledged for their financial support of this work through Labex SEAM (Science and Engineering for Advanced Materials and Devices) (ANR 11 LABX 086 and ANR 11 IDEX 05 02). The authors are grateful to Dr. J. S. Lomas (Paris Diderot University) for his scientific advice and Dr. S. Nowak (Paris Diderot University) for her technical assistance during XRD and XRF experiments.

Conflict of Interest

The authors declare no conflict of interest.

Keywords

composite, exchange-bias, FORCs, nanoferrites, polyol process

Received: March 7, 2018
Revised: April 24, 2018
Published online:

- [1] a) A. J. Lewis, *J. Am. Ceram. Soc.* **2000**, *83*, 2341; b) J. H. Fendler, F. C. Meldrum, *Adv. Mater.* **1995**, *7*, 607; c) J. H. Fendler, *Chem. Eng.* **2001**, *18*, 1; d) Y. Liu, A. Yuan, G. Zhu, C. Bao, R. Zhang, X. Chen, *Funct. Mater. Lett.* **2014**, *7*, 1450024.
- [2] J. Hu, M. Chen, L. Wu, *Polym. Chem.* **2011**, *2*, 760.
- [3] a) A. G. Kolhatkar, A. C. Jamison, D. Litvinov, R. C. Willson, T. R. Lee, *Int. J. Mol. Sci.* **2013**, *14*, 15977; b) B. Cruz-Franco, T. Gaudisson, S. Ammar, A. M. Bolarin-Miro, F. Sanchez de Jesus, F. Mazaleyrat, G. Vazquez-Victorio, R. Ortega-Zempoalteca, R. Valenzuela, *IEEE Trans. Magn.* **2014**, *50*, 2800106.
- [4] a) D. Li, R. B. Kaner, *J. Mater. Chem.* **2007**, *17*, 2279; b) B. Xu, G. Zhou, X. Wang, *NPG Asia Mater.* **2015**, *7*, e164.
- [5] J. Nogués, J. Sort, V. Langlais, V. Skumryev, S. Suriñach, J. S. Muñoz, M. D. Baró, *Phys. Rep.* **2005**, *422*, 65.
- [6] a) T. Gaudisson, L. Ourry, H. Hammoud, N. Menguy, N. Yaacoub, J. M. Grenèche, F. Mammeri, S. Ammar, *J. Nanopart. Res.* **2014**, *16*, 2359; b) W. Baaziz, B. P. Pichon, C. Lefevre, C. Ulhaq-Bouillet, J. M. Grenèche, M. Toumi, T. Mhiri, S. Begin-Colin, *J. Phys. Chem. C* **2013**, *117*, 11436; c) S. Chandra, A. Biswas, H. Khurshid, W. Li, G. C. Hadjipanayis, H. Srikanth, *J. Phys.: Condens. Matter* **2013**, *25*, 426003.
- [7] a) G. Salazar-Alvarez, J. Sort, S. Suriñach, M. D. Baró, J. Nogués, *J. Am. Chem. Soc.* **2007**, *129*, 9102; b) Y. Hu, Y. Liu, A. Du, *J. Magn. Mater.* **2011**, *323*, 2613; c) N. F. Troitiño, B. Rivas-Murias, B. Rodríguez-González, V. Salgueiriño, *Chem. Mater.* **2014**, *26*, 5566.
- [8] a) O. Crisan, A. D. Crisan, *J. Alloys Compd.* **2011**, *509*, 652; b) J. Sort, J. Nogués, X. Amils, S. Suriñach, J. S. Muñoz, M. D. Baró, *Appl. Phys. Lett.* **1999**, *75*, 3177; c) T. F. Marinca, B. V. Neamtu, I. Chicinaş, O. Isnard, *J. Alloys Compd.* **2014**, *608*, 54; d) L. del Bianco, D. Fiorani, A. M. Testa, E. Bonetti, L. Signorini, *Phys. Rev. B* **2004**, *70*, 052401; e) L. del Bianco, D. Fiorani, A. M. Testa, *J. Magn. Mater.* **2007**, *310*, 2289.
- [9] a) V. Skumryev, S. Stoyanov, Y. Zhang, G. Hadjipanayis, D. Givord, J. Nogués, *Nature* **2003**, *423*, 850; b) B. Kuerbanjiang, U. Wiedwald, F. Haring, J. Biskupek, U. Kaiser, P. Ziemann, U. Herr, *Nanotechnology* **2013**, *24*, 455702; c) A. Fischer, R. Kruk, D. Wang, H. Hahn, *Beilstein J. Nanotechnol.* **2015**, *6*, 1158.
- [10] a) J. P. van der Zaag, A. R. Ball, L. F. Feiner, R. M. Wolf, P. A. A. van der Heidjen, *J. Appl. Phys.* **1996**, *79*, 5103; b) P. J. van der Zaag, Y. Ijiri, J. A. Borchers, L. F. Feiner, R. W. Wolf, J. M. Gaines, R. W. Erwin, M. A. Verheijen, *Phys. Rev. Lett.* **2000**, *84*, 6102; c) Y. Ijiri, T. C. Schulthess, J. A. Borchers, P. J. van der Zaag, R. W. Erwin, *Phys. Rev. Lett.* **2007**, *99*, 147201; d) C. A. Kleint, M. K. Krause, R. Höhne, T. Walter, H. C. Semmelhack, M. Lorenz, P. Esquinazi, *J. Appl. Phys.* **1998**, *84*, 5097.
- [11] H. Basti, L. Ben Tahar, L. S. Smiri, F. Herbst, M. J. Vaulay, F. Chau, S. Ammar, S. Benderbous, *J. Colloid Interface Sci.* **2010**, *341*, 248.
- [12] T. Gaudisson, R. Sayed-Hassan, N. Yaacoub, G. Franceschin, S. Nowak, J.-M. Grenèche, N. Menguy, Ph. Sainctavit, S. Ammar, *CrystEngComm* **2016**, *8*, 3799.
- [13] F. Fiévet, in *Fine Particles: Synthesis, Characterization and Mechanism Growth* (Ed: T. Sugimoto), Marcel Dekker, New York **2000**.
- [14] D. Peddis, N. Yaacoub, M. Ferretti, A. Martinelli, G. Piccaluga, A. Musinu, C. Cannas, G. Navarra, J.-M. Grenèche, D. Fiorani, *J. Phys.: Condens. Matter* **2011**, *23*, 426004.
- [15] A. Doriguetto, N. Fernandes, A. Persiano, E. N. Filho, J.-M. Grenèche, J. D. Fabris, *Phys. Chem. Miner.* **2003**, *30*, 249.
- [16] N. Guigue-Millot, N. Keller, P. Perriat, *Phys. Rev. B* **2001**, *64*, 012402.
- [17] G. A. Petitt, D. W. Forester, *Phys. Rev. B* **1971**, *4*, 391.
- [18] R. S. Hassan, T. Gaudisson, N. Yaacoub, J.-M. Grenèche, N. Menguy, N. Nedelka, A. Slawaska-Waniewska, M. Galmiche, F. Mammeri, S. Ammar, *Mater. Res. Express* **2014**, *1*, 025035.
- [19] R. Valenzuela, S. Ammar, F. Herbst, R. Ortega-Zempoalteca, *Nanosci. Nanotechnol. Lett.* **2011**, *3*, 598.
- [20] E. De Biasi, J. Curiale, R. D. Zysler, *J. Magn. Mater.* **2016**, *419*, 580.
- [21] a) *Solids Far from Equilibrium* (Ed: C. Godrèche), Cambridge University Press, Cambridge **1991**; b) *Dynamics of Fractal Surfaces* (Eds: F. Family, T. Vicsek), World Scientific, Singapore **1991**.
- [22] a) C. Herring, *Structure and Properties of Solid Surfaces* (Eds: R. Gomer, C. S. Smith), University of Chicago Press, Chicago, IL **1953**; b) J. K. Mackenzie, A. J. W. Moore, J. F. Nicholas, *J. Phys. Chem. Solids* **1962**, *23*, 185; c) J. A. Venables, *Introduction to Surface and Thin Film Processes*, Cambridge University Press, Cambridge **2000**; d) J. E. Taylor, J. W. Cahn, C. A. Handwerker, *Acta Metall. Mater.* **1992**, *40*, 1443.
- [23] a) V. Gorshkov, A. Zavalov, V. Privman, *Langmuir* **2009**, *25*, 7940; b) I. Sevonkaev, V. Privman, *World J. Eng.* **2009**, *6*, 909; c) V. Gorshkov, V. Privman, *Physica E* **2010**, *43*, 1; d) V. Gorshkov, O. Zavalov, B. P. Atanassov, V. Privman, *Langmuir* **2011**, *27*, 8554; e) V. Privman, V. Gorshkov, O. Zavalov, *Heat Mass Transfer* **2014**, *50*, 383.
- [24] a) Q. Zhang, S.-J. Liu, S.-H. Yu, *J. Mater. Chem.* **2009**, *19*, 191; b) B. S. Youmbi, S. K. Sharma, T. Gaudisson, S. Nowak, N. Menguy, F. Calveyrac, S. Ammar, *J. Phys. Chem.* **2018** (submitted).
- [25] L. Poul, S. Ammar, N. Jouini, F. Fiévet, F. Villain, *J. Sol-Gel Sci. Technol.* **2003**, *26*, 261.
- [26] L. Lutterotti, S. Matthies, H. R. Wenk, *IUCr CPD Newsllett.* **1999**, *21*, 14.
- [27] C. R. Pike, A. P. Roberts, K. L. Verosub, *J. Appl. Phys.* **1999**, *85*, 6660.
- [28] R. J. Harrison, J. M. Feinberg, *Geosystems* **2008**, *9*, 11.